2 Basic concepts

In this chapter a brief overview of the observer states, the method used to study these states and the underlying material system will be given. The states, which have been employed as an observer for the electronic and magnetic properties, are the image-potential states. They are unoccupied surface states and therefore two-photon photoemission was chosen as a method to examine them. Due to the spin-sensitive detection, the experiment is ideally suited for ferromagnetic systems. In this work ultrathin iron and cobalt layers grown on Cu(100) were investigated.

2.1 Image-potential states

2.1.1 Binding energy

The existence of image-potential states can be explained by basic electrostatics. When an electron is in front of a metallic surface, an electric field on the vacuum side is induced, which can be described by introducing a positive charge in the metal opposite to the electron (see Figure 2.1). From the electric field an attractive force can be derived, which is given by

$$F(z) = -\frac{e^2}{4\pi\varepsilon_0}\frac{1}{(2z)^2}. \tag{2.1}$$

The factor 2 in the denominator arises due to the distance of $2z$ from the electron to its image charge. The corresponding attractive potential, the so-called image potential, can be directly deduced

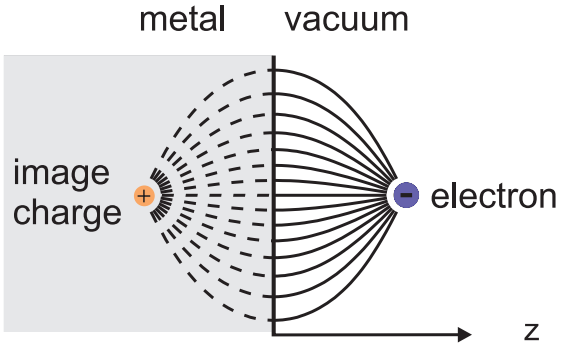

Figure 2.1: *Electric field created by an electron in front of a metal and its equivalence to a dipole-field with the positive charge at a distance $-z$ to the surface.*

$$V(z) = E_{vac} - \frac{e^2}{4\pi\varepsilon_0}\frac{1}{4z} \qquad (z > 0), \tag{2.2}$$

where E_{vac} denotes the vacuum level. Solving the Schrödinger equation of this potential leads to a Rydberg-like series of quantum states, the so-called image-potential states [*Echenique and Pendry*, 1978], whose energy with respect to the quantum number n is given by

$$E_n = E_{vac} - \frac{0.85\ \text{eV}}{n^2} \qquad n = 1, 2, \ldots. \tag{2.3}$$

Note that 0.85 eV is 1/16 Ry and the difference to the hydrogen atom simply arises due to the factor 2 in the denominator in Equation 2.1. This also causes an expansion of the wave function by a factor 4 in comparison to the radial part of the hydrogen wave function beside a multiplication of z due to the reduced dimension [*Echenique and Pendry*, 1990, *Straub and Himpsel*, 1986]. As evident from Figure 2.2 the maximum of the density probability is about 2 Å and 10 Å in front of the surface for the n=1 and n=2 state, respectively.

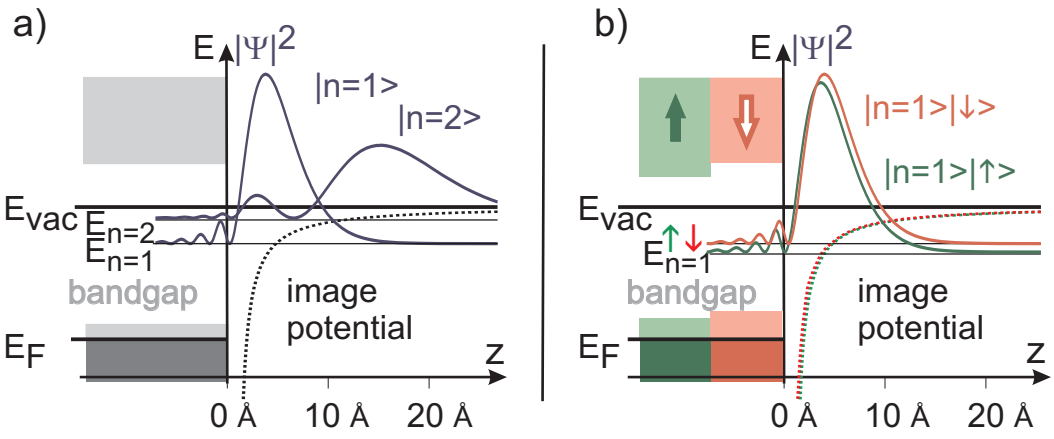

Figure 2.2: *Image-potential, image-potential-state binding energy and wave function. Figure a) refers to a paramagnet, Figure b) to a ferromagnet.*

So far we have assumed the potential inside the metal to be infinite. In reality a band gap in the surface-projected band-structure is sufficient for the existence of surface states [1]. In the band gap the solution of the Schrödinger equation is an exponentially decaying wave function, which has to be matched to the solution of the image potential in the vacuum. The finite penetration of the image-potential-state wave-function into the bulk also changes its binding energy.

[1] If the surface wave-function can couple to bulk wave-functions then one would speak of a surface resonance.

The modification of the binding energy is, e.g., obtained by solving the phase shift model [*Echenique and Pendry*, 1978, 1990, *McRae*, 1979]. Here, the electron wave-function is assumed to be repeatedly reflected at the crystal- and surface-potential barrier with an energy-dependent phase shift. Only for energies, where the sum of the two phase shifts equals an integer multiple of π a solution is obtained. This leads to a modification of the binding energy and Equation 2.3 may now be written as

$$E_n = E_{vac} - \frac{0.85 \text{ eV}}{(n+a)^2} \qquad n = 1, 2, \ldots . \tag{2.4}$$

The so-called quantum defect a is related to the energetic position of the image-potential state within the band gap [*Smith*, 1985]. It rises from 0 at the upper edge of the gap to 0.5 at the lower edge.

Due to the small overlap with the bulk the dispersion of image-potential states is free-electron like and the binding energy including now the parallel momentum k_x and k_y is given by

$$E_n = E_{vac} - \frac{0.85 \text{ eV}}{(n+a)^2} + \frac{\hbar^2(k_x^2 + k_y^2)}{2m_e} \qquad n = 1, 2, \ldots . \tag{2.5}$$

Further details about image-potential states can be found in [*Fauster and Steinmann*, 1995] and [*Steinmann and Fauster*, 1995].

2.1.2 Dynamic properties

Although the dynamics of image-potential states is not in the center of this work, a short survey has to be given. The lifetime of electrons in image-potential states are connected to the lifetime of excited electrons in the crystal at the corresponding energy by the overlap of the image-potential states with the bulk [*de Andrés et al.*, 1987, *Wolf et al.*, 1996]. This leads to a $(n+a)^3$ dependence of the lifetime on the quantum number, which was experimentally verified for $n > 2$ on Cu(100) [*Shumay et al.*, 1998]. Typically, lifetimes are larger than 5 fs and thus accessible in time-resolved measurements employing femtosecond laser-pulses. Therefore these states are often used as model states for studying electron dynamics in metals [*Fauster et al.*, 2006].

When discussing dynamic properties one has in general to distinguish between two terms:

- *Decay:* This refers to a decay of the population and is caused by electron-electron scattering or elastic scattering with the final state being a bulk state or another surface state [*Boger et al.*, 2004].

- *Dephasing:* In this case a phase relation between two states is perturbed, which has initially been built up, e.g., by a laser pulse. Microscopic origin of this process is on the one hand inelastic decay process and on the other hand elastic or quasi-elastic scattering processes with phonons [*Knoesel et al.*, 1998], defects [*Weinelt et al.*, 1999] or adsorbates [*Reuß et al.*, 1999]. The loss of energy is small compared to the experimental energy resolution, which obscures the decay process but the contribution to the dephasing is still visible.

More about electron dynamics of image-potential states can be found in [*Weinelt*, 2002]. A survey about electron dynamics in metals in general was written by [*Echenique et al.*, 2004].

2.1.3 Image-potential states on ferromagnetic surfaces

In ferromagnetic materials the electronic ground state is described by an exchange splitting of the states according to their spin quantum number. Electrons with spin antiparallel to the magnetization direction, also called majority electrons, are energetically lower than electrons with parallel alignment (minority electrons). This leads to an exchange splitting of the band gap and thus causes a spin dependence of the quantum defect and therefore also of the binding energy (see Figure 2.2). The difference between minority and majority binding energy of the image-potential states can again be defined as an exchange splitting.

By using the phase-shift model a maximum exchange splitting of 100 meV was estimated [*Himpsel*, 1991, *Borstel and Thörner*, 1987] depending on the exchange splitting of the bulk bands and the relative position of the image-potential states within the band gap. With a near-surface embedding method the individual contributions from the bulk and surface barrier to the exchange splitting could be distinguished [*Nekovee et al.*, 1993, *Nekovee and Inglesfield*, 1995]. The latter was neglected in the phase-shift model but has only a minor influence in the case of Fe(110).

The first experimental verification with spin-resolved inverse photoemission revealed an exchange splitting of 18± 3 meV for the n=1 state on Ni(111) [*Passek and Donath*, 1992]. A complete survey about exchange-split image-potential states is given by [*Donath et al.*, 2007]. A spin dependence on the lifetime was also found in inverse-photoemission spectroscopy by linewidth analysis and suggested a longer majority- than minority-electron lifetime [*Passek et al.*, 1995].

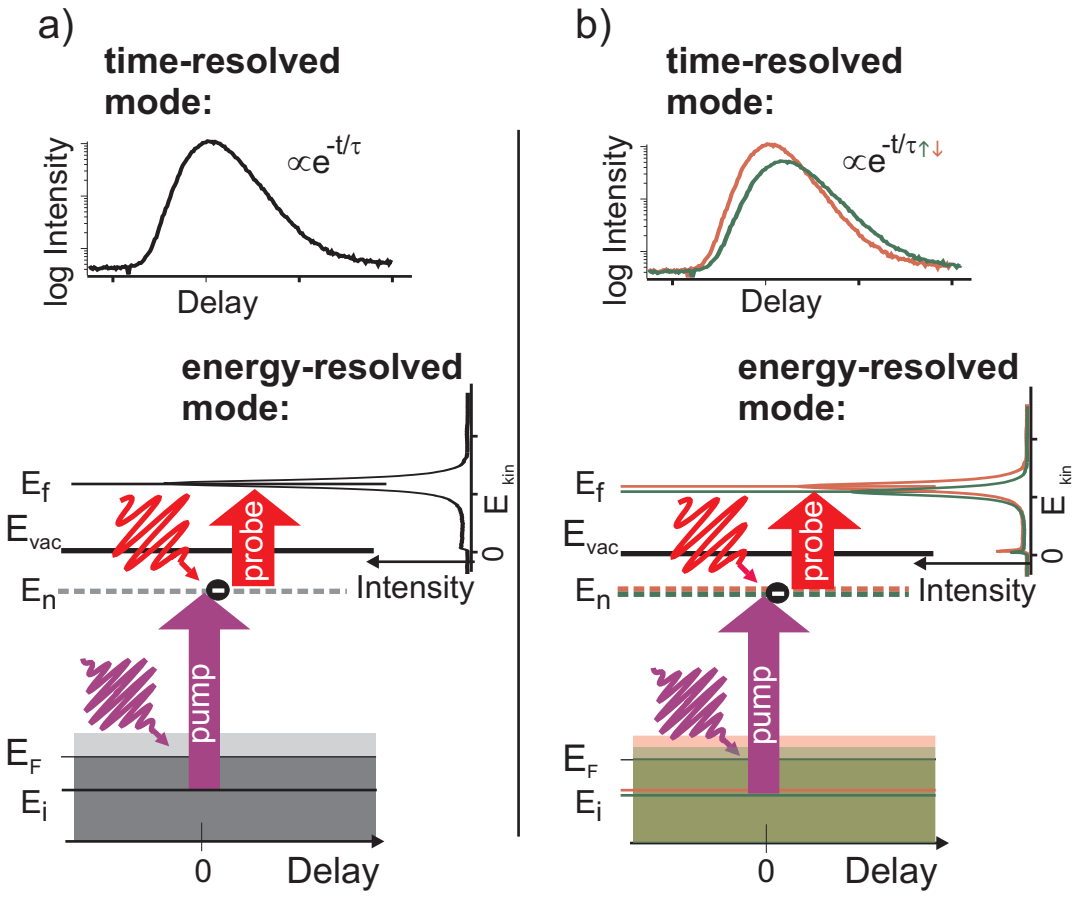

Figure 2.3: *Schematic of 2PPE process with measurement modes for a) spin-integrated and b) spin-resolved spectroscopy.*

2.2 Two-photon photoemission

2.2.1 Principle

An excellent tool to study the energetic as well as dynamic properties of unoccupied surface states, like image-potential states, is two-photon-photoemission spectroscopy (2PPE) [*Fauster and Steinmann*, 1995, *Steinmann and Fauster*, 1995]. In contrast to direct photoemission experiments, 2PPE is based on a two-photon process. The first photon, provided by a laser pulse (pump pulse) excites electrons from an initial state into an unoccupied intermediate state. The second laser pulse (probe pulse) ionizes this state and lifts the electron into the final state, which is above the vacuum level. The electron leaves the crystal and its kinetic energy can be measured with an analyzer. Two different modes of operation exist:

- In the *energy-resolved mode* the delay between the two laser pulses is fixed and a kinetic-energy spectrum of the electrons is recorded (see Figure 2.3).

  The binding energy of the intermediate state can thus be deduced by the kinetic energy E_{kin} of the signal in the spectrum and the photon energy of the probe pulse $h\nu_{probe}$. With respect to the vacuum level it is given by

  $$E - E_{vac} = E_{kin} - h\nu_{probe} \tag{2.6}$$

  or with respect to the Fermi energy E_F by

  $$E - E_F = E_{kin} - h\nu_{probe} + \phi_s, \tag{2.7}$$

  where ϕ_s is the work function of the sample i.e. $E_{vac} - E_F$. Since parts of this work focus on the initial states it is worth to mention that the initial-state energy can simply be calculated by replacing $h\nu_{probe}$ in Equation 2.7 by the sum of the pump- and probe-pulse photon energy $h\nu_{pump} + h\nu_{probe}$.

  Although the set-up would provide the possibility to study the dependence of energetics and dynamics on the parallel component of the wave vector ($k_{||}$), all measurements in this work were performed in normal emission ($k_{||} = 0$). For angle-resolved measurements $k_{||}$ is determined by the kinetic energy and the emission angle θ with respect to the surface normal.

  $$\hbar\, k_{||} = \sqrt{2m_e E_{kin}} \sin\theta. \tag{2.8}$$

- The second mode of operation is the *time-resolved mode*. In this case the kinetic energy of the analyzer is kept constant and the intensity is measured

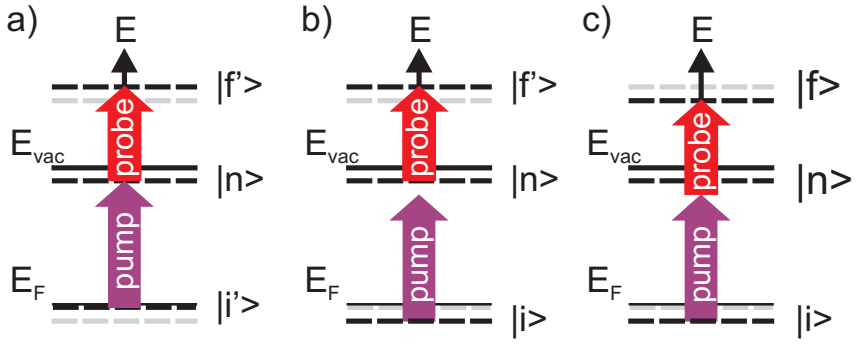

Figure 2.4: *Excitation precesses in two-photon photoemission.* a) *Resonant excitation,* b) *off-resonant excitation in pump process* c) *off-resonant excitation in pump and probe process similar to excitation via a virtual intermediate state.*

as a function of the delay between the two laser pulses. This gives direct access to the transient population in the intermediate state. Simulating the time-resolved measurement with optical Bloch equations (see Section 2.2.2) allows us to derive dynamical properties like the lifetime and the dephasing time.

In the case of 2PPE from a ferromagnetic sample in combination with a spin sensitive detector one can distinguish between majority and minority electrons in both modes. This gives access to spin-dependent binding energies and dynamic properties.

2.2.2 Description by optical Bloch equations

Disregarding indirect excitation processes, three states are of relevance in 2PPE (see Figure 2.4):

- *Initial state* $|i>$: For the initial state usually two scenarios are considered. A discrete initial state, like the Shockley surface state on Cu(111) or a quasi continuum of states like on Cu(100) [*Wolf et al.*, 1999].

- *Intermediate state* $|n>$: In our case only image-potential states have to be considered as intermediate states. Due to the small energetic difference between image-potential states with a quantum number $n > 2$ a coherent excitation occurs. This coherent coupling leads to the formation of a wave packet which manifests in an oscillation in the time-resolved measurement [*Höfer et al.*, 1997] superimposed on the overall decay of the signal. These oscillations are also called quantum beats and are used to determine the energetic difference of the image-potential states up to $n = 7$ [*Höfer et al.*, 1997] or as a measure of the decoherence (dephasing) [*Reuß et al.*, 1999].

- *final state* $|f>$: A continuum of free-electron like final states is always assumed. In the description with the Bloch equations it is chosen as a variable and its energy-dependent occupation resembles the energy-resolved 2PPE spectrum.

Due to the coherent excitation with nearly transform-limited laser pulses the use of simple rate equations is not valid any more. To account for the coherence, energy relaxation, and dephasing a pure quantum mechanical treatment in terms of optical Bloch equations has to be employed [*Hertel et al.*, 1996].

In the unperturbed system the time evolution of each state $|i>, |n>, |f>$ is given by

$$c_j(t)|j>= |c_j(t)|e^{i\phi_j(t)} \cdot e^{i\omega_j t}|j> \tag{2.9}$$

A laser pulse leads to a coupling of the three states $|i>, |n>, |f>$, whose time evolution can be described by the Liouville-von Neumann equation [*Loudon*, 1983].

$$\dot{\hat{\rho}}_{mn} = -\frac{i}{\hbar}\left[\hat{H}_0 + \hat{V}, \hat{\rho}\right]_{mn} - \hat{\Gamma}_{mn}\hat{\rho}_{mn} \tag{2.10}$$

Here, we make use of density matrix formalism [*Blum*, 1983], in which the temporal evolution of the states $|\Psi\rangle = \sum_{j=i,n,f} c_j(t)|j\rangle$ is expressed by the density operator $\hat{\rho}(t) = |\psi\rangle\langle\psi|$. The Hamilton operator is given by the sum of the unperturbed Hamilton operator $\hat{H}_0$ with the laser induced perturbation $\hat{V} = -\hat{\mu}\cdot(\vec{\mathcal{E}}^{pump} + \vec{\mathcal{E}}^{probe})$. $\hat{\mu}$ is the dipole operator and $\vec{\mathcal{E}}$ the electric field of the pump or probe pulse, which is given by the product of the polarization vector $\vec{\epsilon}$, the envelope $\mathcal{E}^k$ and the frequency term $e^{i\omega^k t}$: $\vec{\mathcal{E}^k}(t) = \Re\{\vec{\epsilon^k}\mathcal{E}^k e^{i\omega^k t}\}$[*Boger*, 2004]. To phenomenologically account for dissipative terms the matrix $\hat{\Gamma}$ is introduced .

$$\hat{\Gamma} = \begin{pmatrix} 0 & \frac{\Gamma_n}{2} + \Gamma_n^* + \Gamma_i^* & \Gamma_i^* \\ \frac{\Gamma_n}{2} + \Gamma_n^* + \Gamma_i^* & \Gamma_n & \frac{\Gamma_n}{2} + \Gamma_n^* \\ \Gamma_i^* & \frac{\Gamma_n}{2} + \Gamma_n^* & 0 \end{pmatrix} \tag{2.11}$$

The diagonal elements describe the decay of the population, which is given by the decay rate and can be expressed by the lifetime T_1 by $T_1 = \hbar/\Gamma_1$. [2] The off-diagonal elements refer to the decay of the coupling between the states, which is therefore called dephasing rate and obtained by the sum of half the decay rate and the pure dephasing rate $\Gamma_2 = \Gamma_1/2 + \Gamma^*$. In analogy to the lifetime a dephasing time can be defined by $\Gamma_2 = \hbar/T_2$. The pure dephasing is caused by quasi-elastic processes and inelastic decay is mainly caused by electron-electron scattering as explained in Section 2.1.2. In the above dissipation matrix (see Equation 2.11) only a dephasing rate of the initial and intermediate states is

[2]Note that the subscript 1 in this case does not refer to a certain state but is used to distinguish decay rate from dephasing rate which is labeled with the subscript 2.

assumed. Furthermore, due to the low excitation power the population in the initial state is assumed to stay constant.

For the sake of simplicity we restrict the problem to a simple two-level system consisting of the initial and final state coupled by the pump pulse with envelope $\mathcal{E}(t)$ proposed by [*Hertel et al.*, 1996]. A detailed treatment including all three levels can, e.g., be found in [*Boger*, 2004, *Boger et al.*, 2002]. For the two-level system the decay rate can be expressed by $\Gamma_1 = \Gamma_{nn}$ and the off-diagonal dephasing rate by $\Gamma_2 = \Gamma_{nn}/2 + \Gamma^*_{in}$. Equation 2.10 now leads to the optical Bloch equations in the rotating frame approximation [*Loudon*, 1983]

$$\begin{aligned} \frac{d\rho_{nn}}{dt} &= \frac{\hat{\mu}_{in}(\vec{\mathcal{E}(t)})}{2i\hbar}(\widetilde{\rho}_{in} - \widetilde{\rho}_{ni}) - \frac{\rho_{nn}\Gamma_1}{\hbar} \\ \frac{d\widetilde{\rho}_{in}}{dt} &= \frac{\hat{\mu}_{in}(\vec{\mathcal{E}(t)})}{2i\hbar}(\rho_{nn} - \rho_{ii}) + (i(\omega_{in} - \omega_{pump}) - \frac{\Gamma_2}{\hbar})\widetilde{\rho}_{in} \end{aligned} \tag{2.12}$$

with $\widetilde{\rho}_{in} = \rho_{in}\exp[-i(\omega_{in} - \omega)t]$ and $\omega_{in} = \omega_n - \omega_i$. The following properties can be deduced from the optical Bloch equations:

- After excitation, when $\mathcal{E}(t) = 0$, the dynamics is governed by the exponential decay of the population ρ_{nn} and the coupling ρ_{in}, quantified by the decay rate Γ_1 and the dephasing rate Γ_2.

- For resonant excitation $\omega_{in} = \omega_{pump}$ and for negligible dephasing and decay the two coupled differential equations yield oscillating solutions (Rabi oscillations) resulting in no net excitation of the final state $|n>$. Introducing dephasing Γ_2 leads to a damping in the oscillations of $\widetilde{\rho}_{in}$, which finally results in a population of $|n>$.

- In the case of $\omega_{in} \neq \omega_{pump}$ an oscillation in the coupling term is obtained. This leads to a periodical population and depopulation and therefore an overall net population is considerably hindered. A significant enhancement of the excitation is obtained for $\omega_{in} = \omega_{pump}$ [*Wolf et al.*, 1996]. The two processes, off-resonant and resonant excitation, are shown in Figure 2.4 a) and b).

- As displayed in Figure 2.4 c) also an off-resonant excitation in both 2PPE processes is possible. This requires an overlapping pump and probe pulses. The temporal evolution is equivalent to an autocorrelation trace of the two laser pulses. The most prominent example for this excitation process is given by 2PPE from the occupied Shockley surface state of Cu(111), which gives a clear signature in the spectrum, even if it is not excited via intermediate states.

- *Boger et al.* [2002] have additionally studied the influence of the pulse shape envelope on the linewidth by modeling the energy-resolved spectra with optical Bloch equations. In general, a decrease of the linewidth with increasing

pump-probe delay was observed. For Gaussian shaped pulses and at a large pump-probe delay the linewidth only depends on the dephasing rate in the intermediate state convoluted with the experimental resolution given by the analyzer and the spectral width of the probe pulse. Therefore measurements with large pump-probe delay would be preferable to achieve small linewidths. However, low count rates have to be encountered due to the decay processes.

2.3 Material systems

As already discussed in the previous chapter image-potential states are surface states with small bulk penetration. Therefore their electronic and dynamic properties show a pronounced surface sensitivity. Since the electronic properties depend on the magnetic and geometric structure of the surface a detailed discussion is necessary.

Compared to bulk materials thin ferromagnetic films may exhibit significantly different magnetic properties. The reason for this is the reduced dimensionality and symmetry as well as the change in geometric structure. The latter is strongly influenced by the substrate and often a pseudomorphic growth, i.e. a conservation of the lateral periodicity of the substrate structure, is achieved. Due to the heterogeneity also alloying or inter-diffusion has to be considered. Growth conditions often have a significant influence on these processes. In the next section a survey of the geometric and magnetic structure of the studied systems will be given, followed by a section reporting on their electronic structure.

2.3.1 Geometric and magnetic structure

Fe/Cu(001)

Understanding the interplay between structure and magnetism was and still is one of the driving forces behind studying ultrathin iron films on Cu(100). At room temperature copper has a face-centered cubic (fcc) structure whereas bulk iron crystalizes in a body-centered cubic (bcc) structure (α-Fe). Only at temperatures between 1185 and 1667 K an fcc structure is present (γ-Fe). Due to the small misfit between the lattice constants of these two materials much effort was made to stabilize fcc iron by growth on Cu(100). However, there exists a complex magnetic and structural behavior of epitaxial ultrathin iron films as a function of coverage. As proposed by [*Thomassen et al.*, 1992] and displayed in Figure 2.5 room temperature grown iron films on Cu(100) can be classified in three regions:

- Region I: From 2 to 4 monolayer (ML) the film is ferromagnetic with an *out-of-plane* easy axis of magnetization . Since the magnetization increases linearly with thickness a ferromagnetic structure throughout the film is

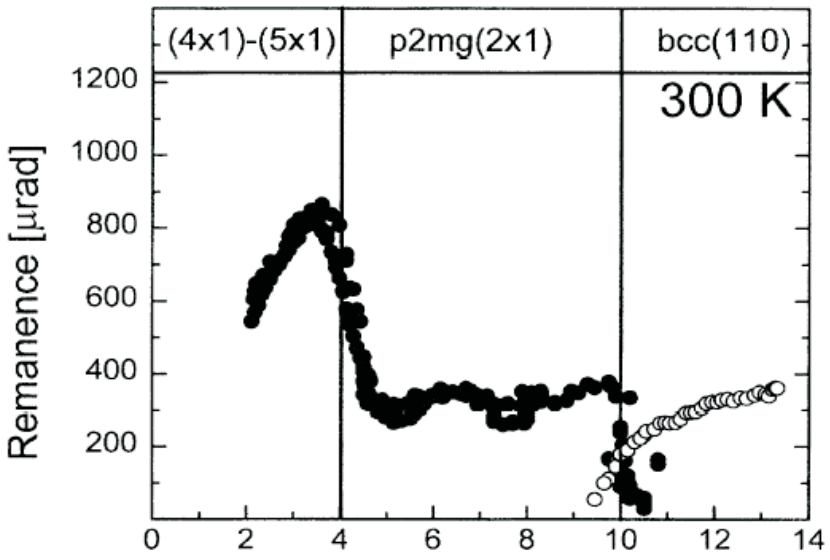

Figure 2.5: *Magnetization as a function of coverage. Taken from [*Müller et al.*, 1995c].*

evident. This has also been confirmed by *ab-initio* calculations based on an fcc arrangement of the film [*Asada and Blügel*, 1997].

While the magnetic structure is widely accepted the geometric structure and its connection to the magnetization is still under discussion. Low energy electron diffraction (LEED) studies revealed a heavily distorted fcc structure with a 4x1 reconstruction for 2 ML forming into 5x1 for 4 ML [*Müller et al.*, 1995c, *Heinz et al.*, 1995, *Müller et al.*, 1995a]. The ferromagnetic behavior was explained by an increased atomic volume. As pointed out later by [*Hammer et al.*, 2004], LEED is not very sensitive to lateral distortions and therefore LEED $I(E)$ curves are also consistent with a locally strained bcc(110)-like reconstruction, which was observed in an atomically resolved scanning tunneling microscopy (STM) experiment [*Biedermann et al.*, 2001b]. The latter was also confirmed by *ab-initio* theory [*Spisak and Hafner*, 2002b]. However, recent studies based on grazing incidence scattering of H and He ions and atoms favor an fcc structure with some distortion for a thickness of 3 monolayer (ML) [*Bernhard et al.*, 2005].

- Region II: From 5 to 10 ML the top two layers are ferromagnetically coupled, and the layers underneath are in an antiferromagnetic (AFM) configuration with a Neel temperature of T=200 K [*Li et al.*, 1994]. This was deduced from the almost constant magnetization obtained by measurements based on magneto-optical Kerr effect (MOKE). An exchange splitting of a crystal-

induced surface state [*Gubanka et al.*, 1996] finally proved the existence of ferromagnetism in the top layers. Further support for an AFM configuration comes from appearance potential spectroscopy [*Popescu et al.*, 2000] Combined STM, LEED and MOKE measurements even supported a non-collinear AFM structure given by a spin-density wave [*Qian et al.*, 2001, *Jin*, 2002]. In contrast, *ab initio* calculations support a ferromagnetic live layer as deduced from experiments with a collinear AFM structure for the layers underneath [*Kraft et al.*, 1994, *Lorenz and Hafner*, 1996, *Spisak and Hafner*, 2002a, *Camley and Li*, 2000]. One has, however, to note that the energetic difference to non-collinear AFM structures is small [*Yavorsky et al.*, 2004] or in the case of odd number of layers coexistence is possible [*Asada and Blügel*, 1997].

Concerning the geometric structure in this region two different models exist. While LEED studies favor an fcc structure with a 2x1 reconstructed top layer [*Müller et al.*, 1995b, *Heinz et al.*, 1999], combined STM and LEED measurements from [*Biedermann et al.*, 2004a,b] revealed an undistorted fcc-like structure with a surface reconstruction which resembles local atomic arrangement of the bcc-like phase. However, *Bernhard et al.* [2005] observed an fcc-like surface reconstruction for clean surfaces by grazing incidence scattering techniques, but also showed that after H_2 adsorption this structure transforms in the bcc-like configuration

A further division of region II in two subregions, namely II(1) and II(2) was proposed by *Qian et al.* [2002] and *Jin* [2002]. 5 - 8 ML corresponds to the former region II, whereas from 9 - 11 ML the fcc structure turned out to be unstable against cooling by the irreversible appearance of needles and a concomitant *in-plane* magnetization. Previous measurements already localized these structures and interpreted them as misfit dislocation [*Shen et al.*, 1998b]. Atomically resolved STM studies revealed their bcc-like structure and considered them as a nucleation state for the transition from the fcc- to the bcc-structure [*Biedermann et al.*, 2001a].

- Region III: Above 10 ML the easy axis of magnetization is *in-plane* and the structure is bcc with a (110) orientation on the Cu(100) substrate [*Wuttig et al.*, 1993]

Especially for region I and region II no undisputable geometric configuration is found and the problem whether the FM state can be explained by the existence of a bcc-like or an expanded fcc-like structure remains. Furthermore, a short discussion on the growth mode and growth condition is necessary, since both influence the structure as well. The first two monolayer grow simultaneously while for 2-10 ML a layer-by-layer growth is seen by medium energy electron diffraction (MEED) [*Kief and Egelhoff*, 1993, *Thomassen et al.*, 1992] and STM [*Giergiel et al.*, 1995]. Above 11 ML a three-dimensional growth mode takes

over due to misfit dislocations at the transition from the fcc to the bcc-structure [*Thomassen et al.*, 1992]. Parameters which influence the growth mode and the structure are the deposition rate, post annealing, the substrate temperature and the use of surfactants:

- For deposition rates below 0.5 ML/min the simultaneous growth of the first and second layer converts into a layer-by-layer growth [*Man et al.*, 2001b] as observed by LEED- and RHEED-intensity oscillations. These studies also proved a concomitant lowering of the remanence, the coercivity and the Curie temperature.

- Low-energy ion scattering experiments showed that iron films with a coverage of 6 ML are stable against annealing for temperatures up to 420 K while for a 2 ML film an enrichment of substrate atoms at the surface can already be observed for mild annealing temperatures [*Memmel and Detzel*, 1994]. STM studies on a 3 ML iron film revealed that copper substrate atoms diffuse on top of the surface via pinholes [*Shen et al.*, 1995, 1996]. A strong influence on the structure was found for annealing a 5 ML thick film to 490 K. LEED analysis reveals a transition from a tetragonally distorted face-centered structure (fct) to a fcc structure in the inner layers with concomitant reduction in magnetization and Curie temperature, observed with MOKE [*Shen et al.*, 1998a]

- The film reconstruction is very sensitive to residual gases like H_2 or CO. This can be exploited to stabilize certain structures like the fcc structure in region II up to 60 ML by using the surfactant CO [*Thomassen et al.*, 1992, *Kirilyuk et al.*, 1996]

- The above discussion is only valid for room temperature grown films. For iron films grown on Cu(100) at lower temperatures SMOKE measurements showed that region II is becoming smaller and eventually disappears at growth temperatures below 200 K [*Li et al.*, 1994].

As evident from all the studies outlined above ultrathin iron films on copper are by far not simple model systems. Therefore results have to be crosschecked and interpreted carefully.

Co/Cu(001)

Due to the small lattice mismatch cobalt growth pseudomorphic on Cu(100) [*Cerdá et al.*, 1993]. The easy axis of magnetization is *in-plane* along the [110] direction (see e.g. [*Weber et al.*, 1996]).

For the first two monolayer a predominant bilayer growth is observed with STM and X-ray photoemission scattering, which turns over in an almost perfect layer-by-layer growth [*Schmid and Kirschner*, 1992, *Li and Tonner*, 1990].

By reducing the deposition rate, layer-by-layer growth takes over for the first two monolayer as seen by STM and reflection of high energy electrons (RHEED) [*Fassbender et al.*, 1997, *May et al.*, 1997]. The influence of the substrate temperature on the growth mode was studied by [*Bernhard et al.*, 2003]. With grazing incidence scattering of He atoms at substrate temperatures below 300 K a bilayer growth mode for the first two monolayer could be observed. Theory could interpret this behavior as an interplay between transport and exchange processes [*Pentcheva and Scheffler*, 2000].

As for ultrathin iron films on Cu(100) also cobalt thin films are unstable upon annealing. Theoretical investigations showed that a Cu adlayer on top of the cobalt film is energetically much more favorable [*Pentcheva and Scheffler*, 2000] and a diffusion processes during growth is only hindered by kinetics. Heating to 400° C (for 20 ML Co/Cu(100)), however, results in diffusion of Cu atoms through the cobalt film, which form a flat top layer on the Co film [*Li and Tonner*, 1990]. STM experiments identified these diffusion process to occur via pinholes [*Schmid et al.*, 1993]. Moreover, STM and LEED studies identified a c(2x2) alloy structure upon annealing a monolayer Co film to 180° C [*Nouvertné et al.*, 1999]

Compared to ultrathin iron films on copper, ultrathin cobalt is easier to handle. Care has anyway to be taken in annealing processes, which can lead besides of a smoothing of the film to an unwanted alloying or copper capping.

2.3.2 Electronic structure and dipole selection rules

Although the crystal structure for 3 ML Fe/Cu(100) is not unequivocally solved we will assume an fcc structure in the proceeding discussions. Since all measurements were performed on the (100) surface in normal emission it is sufficient to consider only the electronic states lying along the corresponding direction (Δ) in the Brillouin zone (see Figure 2.6 a). In the non-relativistic limit, where spin-orbit coupling is not considered, the symmetry of these states is described by the C_{4v} point-group in the Schönflies notation and the electronic states can be classified in four 1-dimensional representations ($\Delta_1, \Delta_{1'}, \Delta_2, \Delta_{2'}$) and one 2-dimensional representation (Δ_5) (see e.g. [*Cornwell*, 1984]). Additionally, the spin in these states can be treated separately and is classified in majority and minority spin. Wave functions with Δ_1 symmetry transform as the z-axis (perpendicular to the surface). The image-potential states belong to this representation, as well as the final free vacuum state for normal emission.

The band structure of fcc iron and cobalt along the Δ direction, taken from [*Mankey et al.*, 1993, *Fauster*, 2006], is shown in Figure 2.6b. It was calculated for fcc iron by the combined interpolation scheme [*Smith*, 1979] with critical input parameters which were taken from the experiment [*Mankey et al.*, 1993]. To adapt the band structure to fcc cobalt a shift of 0.4 eV of the Fermi level was included [*Thomann*, 1999], which can phenomenologically be justified by the larger number of electrons in cobalt than in iron. This similarity can also

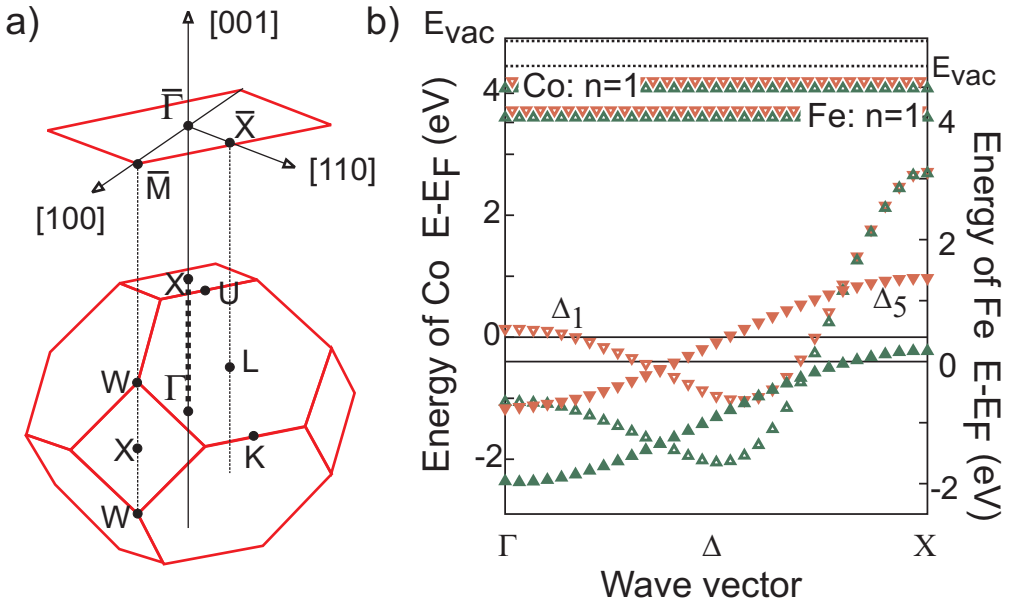

Figure 2.6: *Left: Brillouin zone of an fcc crystal. The dashed line between the points* Γ *and* X *corresponds to a wave vector perpendicular to the (100) surface. Right: The electronic band structure of fcc Fe and fcc Co (left and right energy scale) after [*Mankey et al.*, 1993]. Open symbols denote* Δ_1*-type states, closed symbols* Δ_5*-type states.*

explicitly be seen by a comparison to the calculated band structures in reference [*Mankey et al.*, 1993].

The bands with a strong exchange splitting (Δ_5 and Δ_1 at the Γ point) correspond to the *d* bands, which are also the origin of the ferromagnetic order for these transition metals. The strong dispersive band with almost no splitting close to the *X* point is derived from *sp* states. In contrast to the bulk *sp* and *d* states, the image-potential states have no defined wave vector perpendicular to the surface and are therefore included in the band structure as a non-dispersive electronic state belonging to the Δ_1 representation. The states with Δ_2 symmetry are not shown in the band structure of Figure 2.6b since they do not contribute to the photoemission signal in the non-relativistic limit, as described in the next paragraph.

For both excitation processes in 2PPE the dipole selection rules have to be fulfilled. They define whether a transition from an initial ψ_i into a final state ψ_f (or intermediate state) is possible or not and can be worked out by calculating the transition matrix element $< \psi_f | \, \vec{A}\vec{p} \, | \psi_i >$, where $\vec{A}$ denotes the vector potential of the electro-magnetic wave and $\vec{p}$ the momentum operator. Two different settings for the pump-pulse polarizations were used: p-polarized light and s-polarized light (see Figure 2.7). In the case of s-polarized light the vector potential has only a component parallel to the surface $\vec{A}_s = \vec{A}_{||}$ whereas in case of p-polarized light

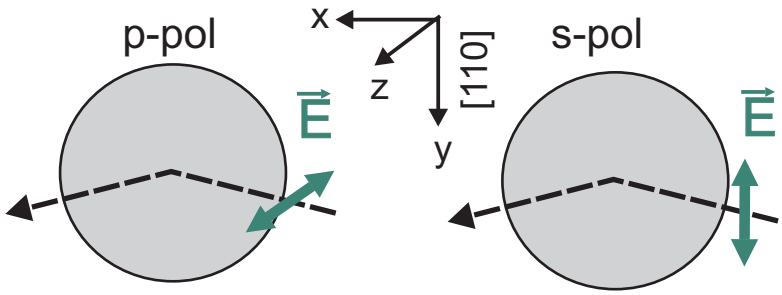

Figure 2.7: *Geometry with p- and s- polarized light. Note that for non-ideal gracing incidence the p-polarized light also exhibits a component parallel to the surface.*

C_{4v}	Δ_1	$\Delta_{1'}$	Δ_2	$\Delta_{2'}$	Δ_5
Δ_1	+	...	...	...	0
$\Delta_{1'}$	...	+	...	...	0
Δ_2	...	...	+	...	0
$\Delta_{2'}$	...	...	...	+	0
Δ_5	0	0	0	0	+

Table 2.1: *Allowed dipole transitions along the Δ direction. (+) denotes A||Δ and (0) for A ⊥ Δ (reproduced from [*Eberhardt and Himpsel, *1980]).*

the vector-potential can be split into a component parallel and perpendicular to the surface $\vec{A}_p = \vec{A}_{||} + \vec{A}_{\perp}$. The ratio of $\vec{A}_{\perp}$ to $\vec{A}_{||}$ for p-polarized light is determined by the angle of incidence with respect to the surface normal (ϑ) by $|\vec{A}_{\perp}| = \sin(\vartheta)|\vec{A}|$ and $|\vec{A}_{||}| = \cos(\vartheta)|\vec{A}|$. Note that this angle reduces due to refraction at the surface. For example the refraction index of a cobalt bulk crystal at a photon energy of 4.5 eV is 1.24 [*Weaver et al.*, 1981], which changes the incidence angle within the bulk from 80° to 53° in our experiment. However, this value refers to the bulk and not the first two or three monolayer. Here we expect a refraction index between the bulk and vacuum value.

The dipole selection rules for an fcc structure along the Δ-direction are given in Table 2.1. For p-polarized light transitions from states with Δ_1 and Δ_5 representation into the image-potential states, which have Δ_1 symmetry are possible. For s-polarized light only Δ_5 states serve as possible initial states in the pump process. In the probe process between the IPS and the final states, both exhibiting Δ_1 symmetry, only p-polarized light allows transitions.

Since the electric field only acts on the spacial part of the wave function, the spin is unaffected in the excitation process, i.e. only spin conserving transitions are possible.